100-Fold Improvement in Carrier Drift Mobilities in Alkanephosphonate-Passivated Monocrystalline TiO_2 Nanowire Arrays

A. Mohammadpour,[1*] B. D. Wiltshire,[1] Y. Zhang,[1] S. Farsinezhad,[1] A.M. Askar,[1] R. Kisslinger,[1] Y. Ren,[1] P. Kar[1] and K. Shankar[1, 2*]

[1]*Department of Electrical and Computer Engineering, University of Alberta, 9211 - 116 St, Edmonton, Alberta, Canada T6G 1H9*

[2]*NRC National Institute for Nanotechnology, 11421 Saskatchewan Dr NW, Edmonton, AB T6G 29*

***Authors to whom correspondence should be addressed:**

1. Arash Mohammadpour (arash3@ualberta.ca)

2. Karthik Shankar (kshankar@ualberta.ca)

Abstract

Single crystal rutile titania nanowires grown by solvothermal synthesis are actively being researched for use as electron transporting scaffolds in perovskite solar cells, in low detection limit ultraviolet photodetectors, in photoelectrochemical water-splitting, and in chemiresistive and electrochemical sensing. The electron drift mobility (μ_n) in solution-grown TiO_2 nanowires is very low due to a high density of deep traps, and reduces performance in optoelectronic devices. In this study, the effects of molecular passivation of the nanowire surface by octadecylphosphonic acid (ODPA), on carrier transport in TiO_2 nanowire ensembles, were investigated using transient space charge limited current measurements. Infrared spectroscopy indicated the formation of a highly ordered phosphonate monolayer with a high likelihood of bidentate binding of ODPA to the rutile surface. We report the hole drift mobility (μ_p) for the first time in unpassivated solvothermal rutile nanowires to be 8.2×10^{-5} $\text{cm}^2\ \text{V}^{-1}\ \text{s}^{-1}$ and the use of ODPA passivation resulted in μ_p improving by nearly two orders of magnitude to 7.1×10^{-3} $\text{cm}^2\ \text{V}^{-1}\ \text{s}^{-1}$. Likewise, ODPA passivation produced between a 2-3 order of magnitude improvement in μ_n from ~10^{-5}-10^{-6} $\text{cm}^2\text{V}^{-1}\text{s}^{-1}$ to ~10^{-3} $\text{cm}^2\text{V}^{-1}\text{s}^{-1}$. The bias dependence of the post-transit photocurrent decays in ODPA-passivated nanowires indicated that minority carriers were lost to trapping and/or monomolecular recombination for small values of bias (< 5 V). Bimolecular recombination was indicated to be the dominant recombination mechanism at higher bias values.

KEYWORDS: self-assembled monolayer, nanorods, bottom-up nanofabrication, electrochemical anodization, nanostructured titania, photoconductivity, solar cells, photoelectrochemical, carrier dynamics.

† Electronic Supplementary Information (ESI) available. see DOI:

1. Introduction

TiO_2 nanowire arrays grown by solvothermal synthesis are *n*-type, vertically oriented, monocrystalline wide-bandgap semiconductor nanostructures made of the rutile phase of titania which also exhibit a high photonic strength [1-4]. The absence of grain boundaries, presence of vectorial charge transport pathways and the formation of ohmic contacts with transparent conducting oxide (TCO) growth substrates make rutile NW arrays (Rut-NWAs) an interesting platform for optoelectronic applications. The strong Mie scattering in the submicrometer high index Rut-NWAs, the comparability of the nanowire and inter-nanowire dimensions to carrier diffusion lengths, and the inherent orthogonalization of charge separation and charge generation/collection processes in high aspect ratio nanorod arrays make Rut-NWAs particularly attractive for light harvesting applications [5-7]. For instance, high performance has been achieved through the use of Rut-NWAs as electron transporting scaffolds in dye-sensitized solar cells, halide perovskite photovoltaics and quantum dot-based depleted heterojunction solar cells [8-13]. Rut-NWA photoelectrodes have shown high activity for sunlight-driven water-splitting and the photocatalytic degradation of organic compounds [14-21]. High gain ultraviolet photodetectors [22, 23], self-powered low response time photodetectors [24, 25] and chemiresistive gas sensors [26] have also been demonstrated using Rut-NWAs. The facile and low-cost solution-based growth process is a further positive attribute from the point of view of mass production and commercialization of Rut-NWA-based devices.

In spite of the technological importance of Rut-NWAs indicated above, fundamental studies of carrier dynamics in Rut-NWAs are severely lacking, which in turn, prevents optimal design and usage of Rut-NWAs in various optoelectronic device applications. For instance, the hole mobility in Rut-NWAs is unknown and the nature of electron-hole recombination processes in Rut-NWAs are a matter of conjecture. Only a handful of reports have attempted to directly quantify electronically relevant parameters in Rut-NWAs. We have previously shown that as-synthesized Rut-NWAs suffer from a high density of deep electron traps, which result in a diminished electron mobility of ~10^{-5}-10^{-6} $cm^2V^{-1}s^{-1}$ [27]. The high surface area of Rut-NWAs automatically engenders a large number of surface defects which act as trapping states ($N_T \geq 10^{16}$ cm^{-3}) [27]. Therefore, a suboptimal compromise is often accepted by choosing a large nanowire width (so as to reduce the number of surface traps/ per unit volume) but thereby also incurring the penalty of greater recombination due to higher retrieval lengths for photogenerated charge carriers. Even after achieving such a compromise, the insidious effects of high trap densities and concomitant low carrier mobilities persist in the form of hysteresis and space-charge limited current effects in the electrical characteristics of solar cells, long response and recovery times in photodetectors and chemiresistive sensors, accelerated recombination in photoelectrochemical cells, etc [28-31]. A proven superior approach is to passivate the surface in order to avoid the aforementioned trade-off and improve optoelectronic device performance [32]. Two generic passivation methods have been reported thus far - (i) the formation by atomic layer deposition of a thin shell of high quality TiO_2 or ZnO coating the Rut-NWAs [14, 19, 33] and (ii) the use of a chemical and/or annealing treatment [34]. To the best of our knowledge, the results of ALD passivation of Rut-NWAs have not been quantitatively measured, and have merely been inferred through performance improvements during empirical testing of the ALD-passivated Rut NWA-based solar cells or photoanodes for water-splitting. On the other hand, chemical/annealing treatments have been demonstrated to reduce the surface state density in Rut-NWAs. The Feng group employed immersion in ammoniacal peroxide followed by annealing at 723 K to achieve a 20 fold improvement in the electron diffusion coefficient [34]. In this report, we utilize a third passivation method, namely the use of a phosphonate self-assembled monolayer (SAM), and demonstrate 2 orders of magnitude improvements in both the electron and hole drift mobilities in Rut-NWAs.

2. Experimental Details

2.1 Fabrication

Fluorine-doped tin oxide (FTO)-coated glass (TEC-15, 15 ohm/square) substrates were first cleaned with detergent followed by thorough rinsing in water, then cleaned in acetone, methanol in an ultrasonic bath and subsequently dried in a nitrogen jet. The substrates were loaded into a 23 mL capacity, sealed Teflon reactor in a PARR acid digestion vessel containing 5 mL of H_2O, 2.5 mL glacial acetic acid and 2.5 mL concentrated HCl. 0.2 mL titanium butoxide was then added drop-by-drop and stirred until a clear solution was obtained. The hydrothermal synthesis was performed at 180°C for 6 hours. The ODPA monolayer was formed by overnight immersion of the nanowire array in 1 mM solution of ODPA in a 4:1 mixture of isopropanol and water.

2.2 Characterization

Morphological and structural characterization were performed using a Hitachi S4800 cold field emission scanning electron microscope and a Hitachi HF3300 transmission electron microscope respectively.

2.3 Time-of-flight and Dark injection studies

Metal electrodes were deposited onto the nanowires through a shadow mask in an electron beam evaporation system. The samples were mounted such that deposition occurred at an oblique angle, in order to minimize the depth of penetration of the deposited metal between the nanowires. Voltage bias was applied between the FTO:glass substrate and the metallic top electrode using a DC power supply. Charge carriers were optically injected into the sample from a nanosecond pulsed N_2 laser (VSL337ND-S, Spectra-Physics) through the FTO:glass substrate which served as the transparent, blocking electrode. Transients were observed at room temperature and ambient air using an Agilent DSO1034B sampling oscilloscope using a terminal resistance of 50 Ω. To enhance our measurements' signal to noise ratio (SNR), 256 single measurements were averaged, which increased the SNR by a factor of 16. The current-voltage characteristics and capacitance of the samples was measured using a Keithley 4200 semiconductor parameter analyzer equipped with a CVU module. For dark injection measurements, application of the voltage step and recording of the dark injection transients were performed using a Keithley 4200 semiconductor parameter analyzer equipped with a Model 4225 ultra-fast pulse measurement unit (PMU). The rise time of the voltage step used was as small as 70 ns.

3. Results and Discussion

3.1 Carrier drift mobilities in unpassivated monocrystalline rutile-phase TiO_2 nanowires

We used time-of-flight (TOF) measurements in the space charge limited current (SCLC) regime, to probe carrier transport in bare (unpassivated) and SAM-coated Rut-NWAs. Such large signal TOF measurements typically yield clear transit times even for dispersive and highly insulating materials [35-37], while such a determination is more ambiguous and often impossible using small signal TOF data. A significant advantage of the TOF technique is its ability to potentially measure the transport characteristics of both majority and minority carriers by merely varying the sign of the bias applied during the drift of charge carriers generated by pulsed optical injection. This is in contrast to methods such as CELIV, steady-state SCLC, IMPS, etc. which describe the behavior of majority charge carriers alone [38, 39]. Finally, transient SCLC measurements are also able to provide significant insights into charge carrier recombination processes [40]. The experimental configuration used for transient SCLC measurements is shown in Figure S1. We supplemented SCLC-TOF measurements with time-resolved photoluminescence and dark injection to obtain a more complete picture of carrier dynamics in Rut-NWAs.

Figure 1a shows the oscilloscope trace obtained from Rut-NWAs grown on fluorine-doped tin oxide (FTO)-coated glass substrates capped with a Ti top electrode. The Ti electrode was deposited on top of the nanowires by oblique angle evaporation to minimize penetration of the metal into the nanowire array. Field emission scanning electron microscope (FESEM) images in Figure S2 indicate oblique angle evaporation to be highly effective in generating intimate contacts to the nanowires while limiting penetration into the inter-nanowire spaces. Illumination of the Rut-NWA through the FTO:glass by a nitrogen laser (337 nm, 4 ns pulse width) generated a high concentration of electron-hole pairs (1.7×10^{21} cm^{-3}) close to the nanowire-FTO interface due to 337 nm photons heavily absorbed by rutile, whose absorption coefficient (α) equals *ca.* 2×10^{5} cm^{-1} @337 nm [41]. Ti generated a blocking contact for electrons in this case. When a positive bias was applied to the Ti electrode, the photogenerated holes were collected almost immediately (at very short time-scales compared to the duration of the experiment) while the electrons drifted through the nanowires and were collected by the Ti electrode.

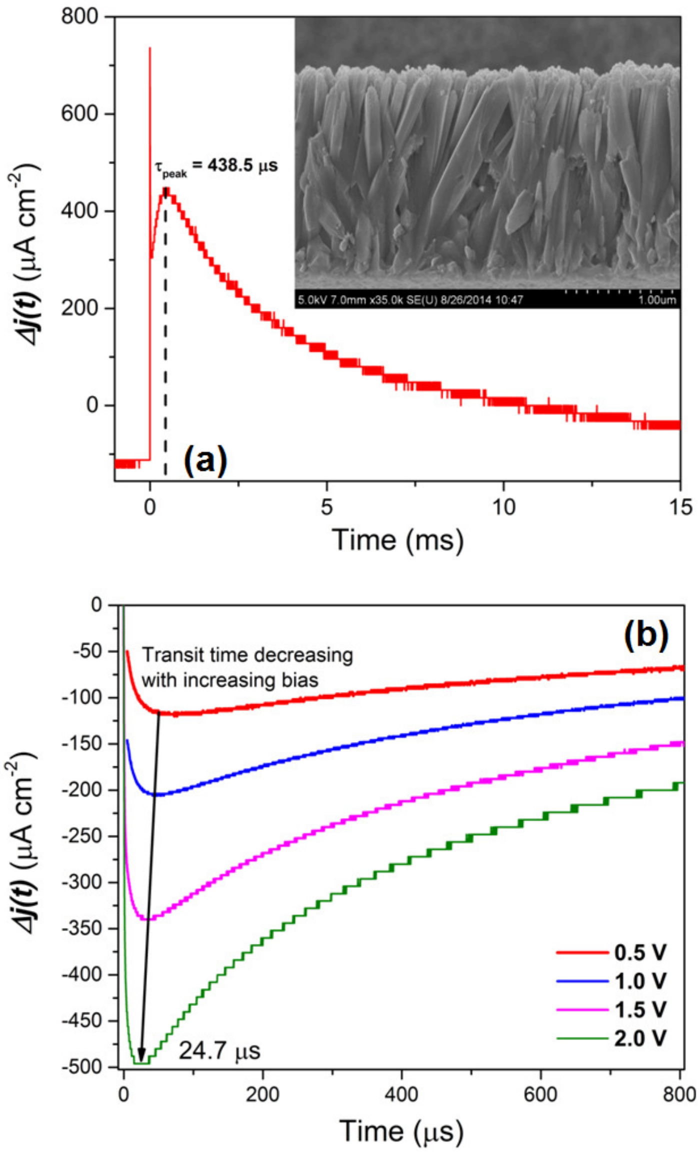

Figure 1. SCLC photocurrent transients for different values of bias following the irradiation of Rut-NWAs by a 4 ns optical pulse from a N_2 laser (a) Electron transit measured using a sample with Ti top metal electrode at a positive potential of 2 V with the inset showing a cross-sectional FESEM image of the morphology of the Rut-NWAs and (b) Hole transit measured using a sample with Al top metal electrode at various negative potentials. In each case, illumination was through the FTO substrate, which was electrically grounded.

A characteristic local maximum or cusp in the transient response for electron transit was observed at 438.5 μs (t_{cusp}) as shown in Figure 1a from which the carrier mobility (μ_n in this case) might be obtained as

$$\mu_n = \frac{Kd^2}{t_{cusp}V} \qquad (1)$$

where d is the distance over which the electrons drift, in turn given by the length of the nanowires minus the penetration depth of the absorbed radiation. V is the bias applied across the nanowires and K is a constant dependent on the ratio (L') of photoinjected charge to the capacitive charge. When L' is unity, K equals 0.786. For the illumination intensity used in our experiment, the value of K was determined to be 0.5 [42]. The electron mobility was found to be 4.6×10^{-6} cm^2 V^{-1} s^{-1} from Equation (1). This value, together with initial value (j_0) and maximum value (j_m) of the transient photocurrent, enabled the setting of a range for μ_n in bare Rut-NWAs of $(4.3 - 7.9) \times 10^{-6}$ cm^2 V^{-1} s^{-1} (see Section S1), in broad agreement with the values reported previously by us and others [27, 43]. In order to observe the transit of holes, an Al top electrode was formed by oblique angle evaporation to ensure a blocking contact for holes. The transient response for holes, shown in Figure 1b, showed transit times inversely proportional to applied bias as expected and the hole drift mobility was estimated to be 8.2×10^{-5} cm^2 V^{-1} s^{-1} in unpassivated Rut-NWAs. Increasing negative bias produces a greater steady-state electron density in the nanowires due to majority carriers injected from the contacts and promotes recombination as manifested through the j_m values decreasing below their theoretical value (See Section S1). The principal reason for the low electron drift mobility and resulting extremely slow electron transport in Rut-NWA devices was found to be a high density of deep-level traps due to surface states [27, 34].

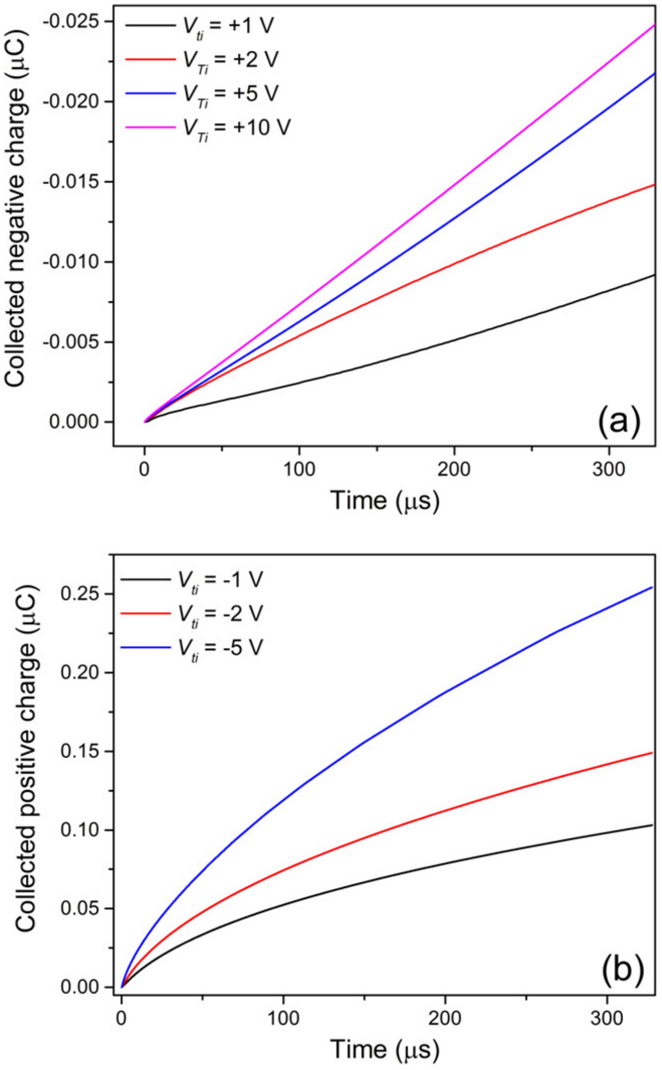

Figure 2. Plots of charge collected vs. time during SCLC-TOF measurements on a Rut-NWA sample with a Ti top electrode for different values of bias for (a) Electrons and (b) Holes. In each case, illumination was through the FTO substrate, which was electrically grounded.

Figure 2 shows the charge collection transients for the Rut-NWAs as a function of bias for a duration of 330 μs following the laser pulse. The much larger number of collected holes (~0.25 C for −5 V bias) vs. collected electrons (~0.022 C for 5 V bias) at similar time-scales provides indirect confirmation of the hole drift mobilities extracted from the TOF measurements (Figure 1) being larger than the corresponding electron drift mobilities. The higher value of the hole drift mobility in comparison to the electron drift mobility implies weaker trapping of holes in comparison to electrons, and is unusual compared to anatase nanoparticles and nanotubes that are characterized by faster and more efficient trapping of holes in comparison to electrons [44, 45].

3.2 Structure and composition of Rut-NWAs

We performed high resolution transmission electron microscopy (HRTEM) to both verify the structure of the nanowires and determine the chemical composition. The lattice fringe spacing of 0.32 nm in Figure 3a (see also Figure S3) corresponds to the (110) crystal plane of the rutile phase of TiO_2. In addition to the expected presence of Ti and O in TEM line scans (see Figure S4), chlorine and carbon were found to be significant impurities homogeneously distributed along the nanowire as shown in Figure 3b. Cl^- ions are adsorbed on to the [110] faces of rutile during the hydrothermal growth process, and the said adsorption process is also responsible for the formation of nanowires. It is however noteworthy that the chlorine impurities survive the rinsing, drying and high vacuum evacuation (for HRTEM) processes the Rut-NWAs were subjected to, indicating chemisorption instead of physisorption. Carbon atoms in the precursors (titanium butoxide, acetic acid) may be incorporated into the rutile lattice in addition to surface adventitious carbon. Cl^- ions and oxygen vacancies are also the likely source of surface states, which explains why the ammoniacal peroxide treatment reported by Sheng et al, was effective in reducing the surface states and improving the transport of majority charge carriers [34].

Figure 4 displays the vibrational spectra for Rut-NWA samples immersed overnight in solutions of ODPA. The Fourier transform infrared (FTIR) spectroscopic data were collected in attenuated total reflectance (ATR) mode in Figure 4 and diffuse reflectance (DRIFTS) mode in the inset of Figure 4. In Figure 4, the symmetric [$\nu_s(CH_2)$] and antisymmetric methylene stretching [$\nu_a(CH_2)$] frequencies for long chain alkyl groups are seen as reflectance troughs at ~2850 cm^{-1} and 2920 cm^{-1} respectively [46], for ODPA-coated Rut-NWAs. The symmetric and antisymmetric stretching frequencies of the terminal CH_3 groups [47] at ~2870 cm^{-1} and 2950 cm^{-1} respectively are faint but observable for ODPA-coated nanowires. The above observations confirm the presence of the ODPA SAMs on the rutile nanowires and also indicate the monolayer to be highly ordered.

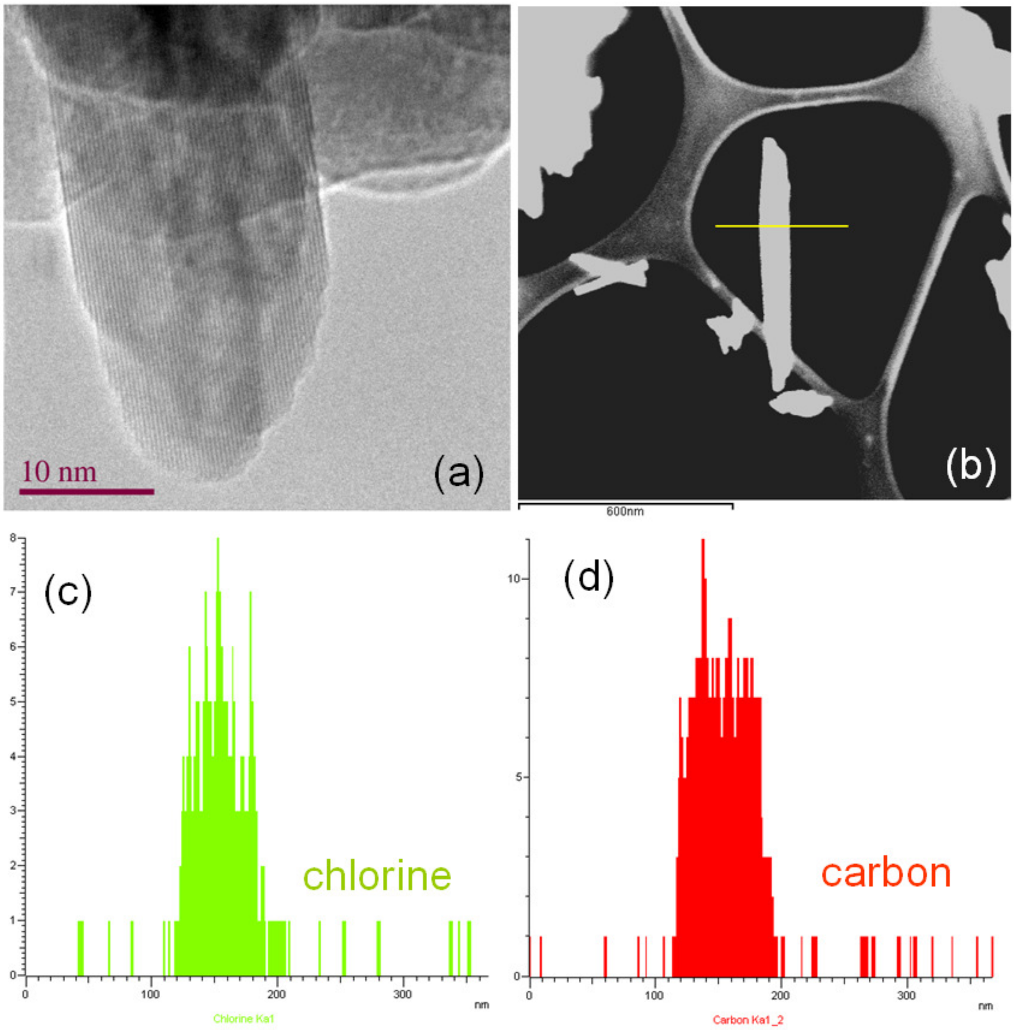

Figure 3. (a) HRTEM image of a single TiO_2 nanowire (b) EDX line scan of a single TiO_2 nanowire showing (c) chlorine content and (d) carbon content along the cross-section of the nanowire.

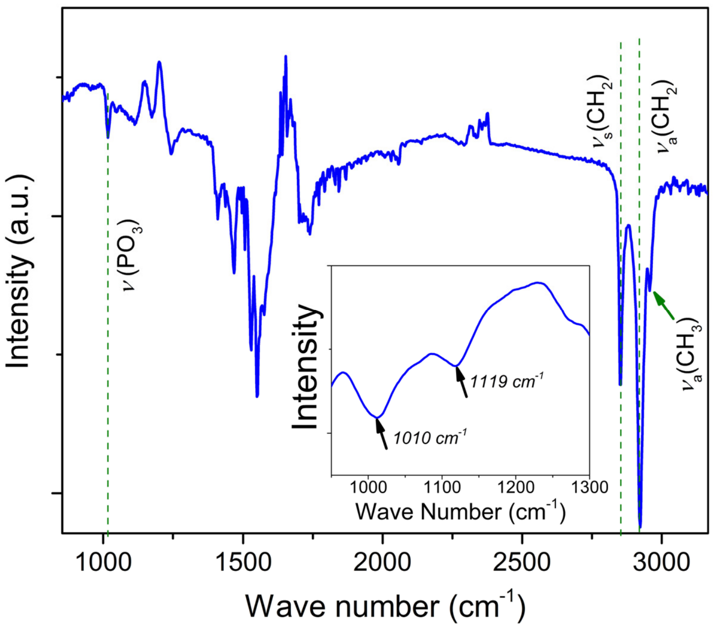

Figure 4. FTIR spectra of SAM-coated Rut-NWAs (a) Collected in ATR mode and (b) Collected in DRIFTS mode. The Inset of (a) is a magnified view of the 2800-3000 cm^{-1} spectral region for NA-coated nanowires.

Hydrogen bonding interactions, differing degrees of metal binding and overlapping absorption peaks of TiO_2 greatly complicate the analysis of the IR spectra of phosphonic acids adsorbed on TiO_2 [48, 49]. Significant dips in the reflectance are observed at the characteristic frequencies (1264 cm^{-1}, 1111 cm^{-1}) for phosphonate binding to TiO_2 [50]. The dips (peaks) corresponding to the P–OH and ν(PO_3) vibrations of unbound ODPA at 1075 cm^{-1} and 950 cm^{-1} are absent in both the ATR spectrum and DRIFTS spectrum of ODPA-rutile TiO_2 while dips corresponding to the ν(P=O) and group ν(PO_3) vibrations of the free acid, albeit very weak in intensity, are still present at 1242 cm^{-1} (red-shifted from 1226 cm^{-1}) and 1012 cm^{-1} respectively [50-53]. These results taken together with the DRIFTS spectrum of ODPA in the inset of Figure 4 which exhibits a trough at 1119 cm^{-1}, attributable to a P=O stretching mode, are strongly suggestive of bidentate bonding to the oxide surface [54]. Furthermore, theory suggests that tridentate binding of phosphonic acids is unstable on the rutile (110) surface in contrast to highly stable monodentate- and bidentate binding configurations [48]. The peaks at 1740 cm^{-1} and

1550 cm^{-1} in the ATR spectrum, close to the positions of C=O and C−O stretches of carboxylate groups may indicate the residual presence of acetate adsorbates from the hydrothermal growth process.

3.3 Carrier dynamics in ODPA-coated Rut-NWAs

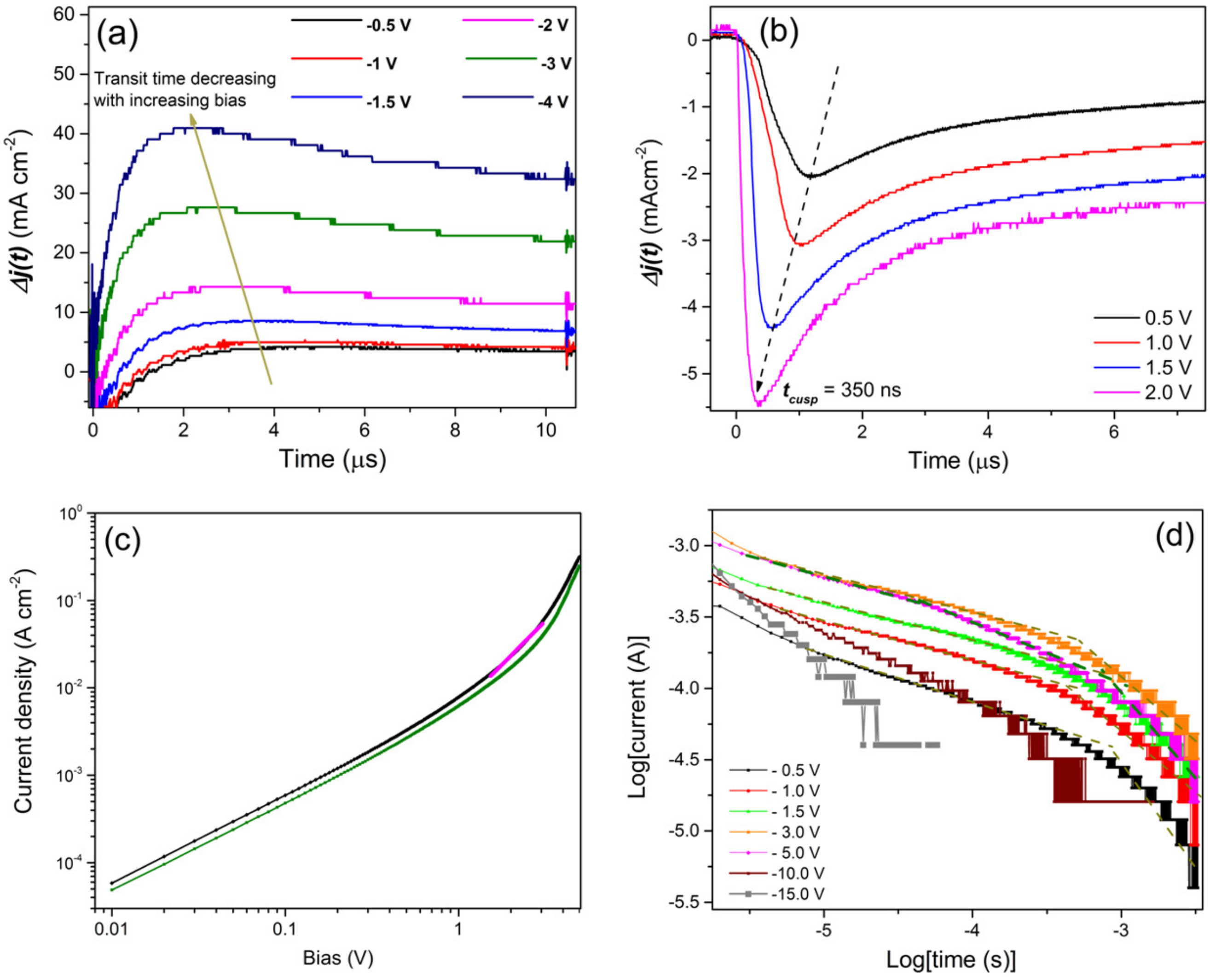

Figure 5. Electrical behavior of ODPA-coated Rut-NWAs (a) SCLC photocurrent transients for electron transit with Pt top metal electrode at positive potentials (b) SCLC photocurrent transients for hole transit with Al top metal electrode at negative potentials (c) Current-voltage characteristics for Pt top metal electrode at positive (black) and negative (green) potentials vs. ground and (d) Post-transit hole extraction transients using ODPA-coated nanowires with Al top metal electrode at negative potentials. For (a), (b) and (c), illumination was through the FTO substrate, which was electrically grounded.

The transient SCLC response plots of ODPA-coated rutile NWs for both positive and negative values of bias, are presented in Figure 5a and Figure 5b respectively. For ODPA-coated rutile NWS, clear cusps for electron transit were obtained with Pt top contacts (Figure 5c). However, clear cusps were not obtained for holes due to the hole transit times being smaller than the system response times (Figure S5). With Al top contacts, the resistance (*R*)-capacitance (*C*) products were small enough for the system *RC* time constants to be smaller than the minority carrier transit times, and clear cusps for holes transit were observed as shown in Figure 5d. The maximum transient space charge limited current $\boldsymbol{\Delta j_{max}}$ increased roughly parabolically with applied bias for positive values of bias (drift of electrons) in Figure 5a (see Section S2) [55]. However, $\boldsymbol{\Delta j_{max}}$ increased sub-parabolically with applied bias for negative bias values because of minority carrier recombination reducing the maximum current. The *J*-*V* characteristics of ODPA-coated Rut-NWAs are plotted on a log-log scale and found to be nearly symmetrical for positive and negative values of bias as seen in Figure 5c. ODPA-coated Rut-NWAs exhibit a long ohmic region in their *J*-*V* characteristic for bias values smaller than 1 V in absolute magnitude which then transitions to a SCLC regime for higher bias values. From the SCLC fit to the *J*-*V* characteristic at positive bias (pink line in Figure 5c), a μ_n value of 2.7×10^{-4} cm^{2}V^{-1}s^{-}1 was extracted using the Mott-Gurney expression while μ_n was extracted to be 4.3×10^{-4} cm^{2}V^{-1}s^{-1} using Equation (1) and the times corresponding to the current maxima in Figure 5a. Dark injection measurements (Section S2 and Figure S6) indicated a slightly higher μ_n value of 2.8×10^{-3} cm^{2}V^{-1}s^{-1} in ODPA-coated NWs. Thus the electron drift mobilities determined using three independent measurements are within roughly an order of magnitude of each other. The μ_p value in ODPA-coated NWs was determined to be 7.1×10^{-3} cm^{2}V^{-1}s^{-1} (Figure 5b). Both the electron- and hole drift mobility values in ODPA-coated Rut-NWAs are nearly two orders of magnitude larger than the corresponding values obtained for bare Rut-NWAs indicating the effective passivation of surface states by long chain alkanephosphonate monolayers. An equilibrium free carrier concentration (n_0) value of 1.3×10^{16} cm^{-3} was obtained from the ohmic region of Figure 5c.

The post-hole-transit photocurrents in Figure 5b and Figure S5, were found to be fit well by biexponential decays consisting of one time constant $\cong 2 \times 10^{-6}$ s and another component $\cong 4 \times 10^{-5}$ s, nearly independent of bias up to a bias of ~ −5 V. We attribute these time constants to characteristic capture times of deep traps and trap-mediated monomolecular recombination. For bias values of ~ 5 V and higher, a noticeable change in character occurs with the appearance of a faster decay component $\cong 4 \times 10^{-7}$ s. Figure 5d shows the post-transit SCLC carrier extraction currents due to their value in providing insights into recombination processes [56, 57]. The change in character of the post-transit photocurrent decays is also observable in Figure 5d wherein two clear breaks in slope are seen for −5 V and much faster decays for bias values of −5 V and higher. Radiative bimolecular recombination is typically dominant for carrier densities of 10^{17}-10^{21} cm^{-3} and is therefore expected in the photoinjected plasma close to the FTO electrode [57]. However, TRPL measurements of ODPA-coated Rut-NWAs at zero bias (not shown) showed a negligibly small PL emission, likely due to the dominance of non-radiative trap-mediated monomolecular recombination and also due to the extremely small value of the bimolecular recombination coefficient ($B \sim 10^{-14}$ cm^{3}s^{-1}) in single crystal rutile [58]. However, as the negative bias on the Al electrode is increased, a higher steady state concentration of electrons in the TiO_2 nanowires is expected due to the injection of majority carriers in the SCLC regime. Consequently, the probability of direct Langevin-type bimolecular recombination of drifting photogenerated holes with steady-state electrons injected from the contact, is enhanced with increasing bias. At −5 V, monomolecular and bimolecular recombination coexist while bimolecular recombination dominates for higher values of bias.

4. Conclusion

The solution-based formation of self-assembled phosphonate monolayers on metal oxide surfaces at low temperatures provides an interesting alternative to ALD passivation. Through the use of ODPA passivating SAMs, we demonstrated nearly 100-fold improvements in both the electron and hole drift mobilities of hydrothermally grown monocrystalline rutile-phase TiO_2 nanowire arrays. The well-known ambient and UV stability of alkanephosphonate monolayers means that phosphonate SAMs offer a route forward to reduce surface traps in TiO_2 nanostructures and improve the performance of TiO_2 nanowire-based photodetectors, photoelectrodes, photovoltaic electron transport layers and photocatalysts.

Acknowledgements

All authors thank NSERC, NRC-Canada, CFI and CMC Microsystems for direct and indirect (equipment) support. A.M., S.F., B.D.W. and A.M.A. thank Alberta Innovates Technology Futures for scholarship support. We acknowledge the role(s) of Kaveh Ahadi, Conrad Vandenbrink and Samuel Muwanguzi in miscellaneous synthesis and characterization tasks related to TiO_2 nanowires. The authors thank the staff at the University of Alberta Nanofab and NRC-NINT with particular thanks to Dr. Kai Cui for assistance with TEM characterization.

References

[1] Feng X J, Shankar K, Varghese O K, Paulose M, Latempa T J and Grimes C A 2008 Vertically Aligned Single Crystal TiO2 Nanowire Arrays Grown Directly on Transparent Conducting Oxide Coated Glass: Synthesis Details and Applications *Nano Lett.* **8** 3781-6

[2] Feng X J, Shankar K, Paulose M and Grimes C A 2009 Tantalum-Doped Titanium Dioxide Nanowire Arrays for Dye-Sensitized Solar Cells with High Open-Circuit Voltage *Angewandte Chemie-International Edition* **48** 8095-8

[3] Liu B and Aydil E S 2009 Growth of Oriented Single-Crystalline Rutile TiO2 Nanorods on Transparent Conducting Substrates for Dye-Sensitized Solar Cells *J. Am. Chem. Soc.* **131** 3985-90

[4] Muskens O L, Diedenhofen S L, Kaas B C, Algra R E, Bakkers E P A M, Gómez Rivas J and Lagendijk A 2009 Large Photonic Strength of Highly Tunable Resonant Nanowire Materials *Nano Lett.* **9** 930-4

[5] Shankar K, Basham J I, Allam N K, Varghese O K, Mor G K, Feng X J, Paulose M, Seabold J A, Choi K S and Grimes C A 2009 Recent Advances in the Use of TiO2 Nanotube and Nanowire Arrays for Oxidative Photoelectrochemistry *J. Phys. Chem. C* **113** 6327-59

[6] Lewis N S 2007 Toward Cost-Effective Solar Energy Use *Science* **315** 798

[7] Liu H F, Huang Z R, Wei S Y, Zheng L L, Xiao L X and Gong Q H 2016 Nano-structured electron transporting materials for perovskite solar cells *Nanoscale* **8** 6209-21

[8] Shankar K, Feng X and Grimes C A 2009 Enhanced Harvesting of Red Photons in Nanowire Solar Cells: Evidence of Resonance Energy Transfer *ACS Nano* **3** 788-94

[9] Kim H-S, Lee J-W, Yantara N, Boix P P, Kulkarni S A, Mhaisalkar S, Grätzel M and Park N-G 2013 High Efficiency Solid-State Sensitized Solar Cell-Based on Submicrometer Rutile TiO2 Nanorod and CH3NH3PbI3 Perovskite Sensitizer *Nano Lett.* **13** 2412-7

[10] Cai B, Zhong D, Yang Z, Huang B K, Miao S, Zhang W H, Qiu J S and Li C 2015 An acid-free medium growth of rutile TiO2 nanorods arrays and their application in perovskite solar cells *J. Mater. Chem. C* **3** 729-33

[11] Li X, Dai S-M, Zhu P, Deng L-L, Xie S-Y, Cui Q, Chen H, Wang N and Lin H 2016 Efficient Perovskite Solar Cells Depending on TiO2 Nanorod Arrays *ACS Appl. Mater. Interfaces* **8** 21358-65

[12] Atomsa Gonfa B, Zhao H, Li J, Qiu J, Saidani M, Zhang S, Izquierdo R, Wu N, El Khakani M A and Ma D 2014 Air-processed depleted bulk heterojunction solar cells based on PbS/CdS core–shell quantum dots and TiO2 nanorod arrays *Sol. Energy Mater. Sol. Cells* **124** 67-74

[13] Gonfa B A, Kim M R, Delegan N, Tavares A C, Izquierdo R, Wu N Q, El Khakani M A and Ma D L 2015 Towards high efficiency air-processed near-infrared responsive photovoltaics: bulk heterojunction solar cells based on PbS/CdS core-shell quantum dots and TiO2 nanorod arrays *Nanoscale* **7** 10039-49

[14] Yun G, Song G Y, Ahn B E, Lee S K, Heo J, Ahn K S and Kang S H 2016 Beneficial surface passivation of hydrothermally grown TiO2 nanowires for solar water oxidation *Appl. Surf. Sci.* **366** 561-6

[15] Su J Z and Guo L J 2015 High aspect ratio TiO2 nanowires tailored in concentrated HCl hydrothermal condition for photoelectrochemical water splitting *RSC Adv.* **5** 53012-8

[16] Wang Y C, Zhang Y Y, Tang J, Wu H Y, Xu M, Peng Z, Gong X G and Zheng G F 2013 Simultaneous Etching and Doping of TiO2 Nanowire Arrays for Enhanced Photoelectrochemical Performance *ACS Nano* **7** 9375-83

[17] Hwang Y J, Hahn C, Liu B and Yang P D 2012 Photoelectrochemical Properties of TiO2 Nanowire Arrays: A Study of the Dependence on Length and Atomic Layer Deposition Coating *ACS Nano* **6** 5060-9

[18] Wang G, Wang H, Ling Y, Tang Y, Yang X, Fitzmorris R C, Wang C, Zhang J Z and Li Y 2011 Hydrogen-Treated TiO2 Nanowire Arrays for Photoelectrochemical Water Splitting *Nano Lett.* **11** 3026-33

[19] Ghobadi A, Ulusoy T G, Garifullin R, Guler M O and Okyay A K 2016 A Heterojunction Design of Single Layer Hole Tunneling ZnO Passivation Wrapping around TiO2 Nanowires for Superior Photocatalytic Performance *Scientific Reports* **6**

[20] Li Y G, Wei X L, Zhu B W, Wang H, Tang Y X, Sum T C and Chen X D 2016 Hierarchically branched Fe2O3@TiO2 nanorod arrays for photoelectrochemical water splitting: facile synthesis and enhanced photoelectrochemical performance *Nanoscale* **8** 11284-90

[21] Song L, Zhao X Y, Cao L X, Moon J W, Gu B H and Wang W 2015 Synthesis of rare earth doped TiO2 nanorods as photocatalysts for lignin degradation *Nanoscale* **7** 16695-703

[22] Selman A M and Hassan Z 2015 Highly sensitive fast-response UV photodiode fabricated from rutile TiO2 nanorod array on silicon substrate *Sensors and Actuators A: Physical* **221** 15-21

[23] Xie Y R, Wei L, Wei G D, Li Q H, Wang D, Chen Y X, Yan S S, Liu G L, Mei L M and Jiao J 2013 A self-powered UV photodetector based on TiO2 nanorod arrays *Nanoscale Research Letters* **8**

[24] Xie Y R, Wei L, Li Q H, Chen Y X, Liu H, Yan S S, Jiao J, Liu G L and Mei L M 2014 A high performance quasi-solid-state self-powered UV photodetector based on TiO2 nanorod arrays *Nanoscale* **6** 9116-21

[25] Wang Z R, Ran S H, Liu B, Chen D and Shen G Z 2012 Multilayer TiO2 nanorod cloth/nanorod array electrode for dye-sensitized solar cells and self-powered UV detectors *Nanoscale* **4** 3350-8

[26] Jin C, Kim H, Choi S W, Kim S S and Lee C 2014 Synthesis, Structure, and Gas-Sensing Properties of Pt-Functionalized TiO2 Nanowire Sensors *J. Nanosci. Nanotechnol.* **14** 5833-8

[27] Mohammadpour A, Farsinezhad S, Wiltshire B D and Shankar K 2014 Majority carrier transport in single crystal rutile nanowire arrays *physica status solidi (RRL) – Rapid Research Letters* n/a-n/a

[28] Fakharuddin A, Di Giacomo F, Palma A L, Matteocci F, Ahmed I, Razza S, D’Epifanio A, Licoccia S, Ismail J, Di Carlo A, Brown T M and Jose R 2015 Vertical TiO2 Nanorods as a Medium for Stable and High-Efficiency Perovskite Solar Modules *ACS Nano* **9** 8420-9

[29] Selman A M and Hassan Z 2016 Fabrication and characterization of metal–semiconductor–metal ultraviolet photodetector based on rutile TiO2 nanorod *Materials Research Bulletin* **73** 29-37

[30] Mihailetchi V D, Wildeman J and Blom P W M 2005 Space-Charge Limited Photocurrent *Phys. Rev. Lett.* **94** 126602

[31] Gagliardi A, Maur M A D, Gentilini D, di Fonzo F, Abrusci A, Snaith H J, Divitini G, Ducati C and Di Carlo A 2015 The real TiO2/HTM interface of solid-state dye solar cells: role of trapped states from a multiscale modelling perspective *Nanoscale* **7** 1136-44

[32] Chang J, Kuga Y, Mora-Sero I, Toyoda T, Ogomi Y, Hayase S, Bisquert J and Shen Q 2015 High reduction of interfacial charge recombination in colloidal quantum dot solar cells by metal oxide surface passivation *Nanoscale* **7** 5446-56

[33] Mali S S, Shim C S, Park H K, Heo J, Patil P S and Hong C K 2015 Ultrathin Atomic Layer Deposited TiO2 for Surface Passivation of Hydrothermally Grown 1D TiO2 Nanorod Arrays for Efficient Solid-State Perovskite Solar Cells *Chem. Mater.* **27** 1541-51

[34] Sheng X, Chen L, Xu T, Zhu K and Feng X 2016 Understanding and removing surface states limiting charge transport in TiO2 nanowire arrays for enhanced optoelectronic device performance *Chemical Science* **7** 1910-3

[35] Isberg J, Hammersberg J, Johansson E, Wikström T, Twitchen D J, Whitehead A J, Coe S E and Scarsbrook G A 2002 High Carrier Mobility in Single-Crystal Plasma-Deposited Diamond *Science* **297** 1670

[36] Kolomiets B and Lebedev E 1973 TRANSIENT SPACE-CHARGE-LIMITED CURRENTS AND MOBILITY IN CHALCOGENIDE GLASSES *Soviet Physics: Semiconductors* **7** 134

[37] Szymański M Z, Łuszczyńska B and Djurado D 2013 Modeling the Transient Space-Charge-Limited Current Response of Organic Semiconductor Diodes Using the Master Equation Approach *IEEE J. Sel. Top. Quantum Electron.* **19** 1-7

[38] Ashraf A, Dissanayake D M N M and Eisaman M D 2015 Measuring charge carrier mobility in photovoltaic devices with micron-scale resolution *Appl. Phys. Lett.* **106** 113504

[39] Wu W-Q, Lei B-X, Rao H-S, Xu Y-F, Wang Y-F, Su C-Y and Kuang D-B 2013 Hydrothermal Fabrication of Hierarchically Anatase TiO2 Nanowire arrays on FTO Glass for Dye-sensitized Solar Cells *Scientific Reports* **3** 1352

[40] Juška G, Kočka J, Viliũnas M and Arlauskas K 1993 Subnanosecond bimolecular non-radiative recombination in a-Si:H *J. Non-Cryst. Solids* **164** 579-82

[41] Park Y R and Kim K J 2005 Structural and optical properties of rutile and anatase TiO2 thin films: Effects of Co doping *Thin Solid Films* **484** 34-8

[42] Juška G, Viliunas M, Klíma O, Šípek E and Kočka J 1994 New features in space-charge-limited-photocurrent transients *Philosophical Magazine Part B* **69** 277-89

[43] Feng X, Zhu K, Frank A J, Grimes C A and Mallouk T E 2012 Rapid Charge Transport in Dye-Sensitized Solar Cells Made from Vertically Aligned Single-Crystal Rutile TiO2 Nanowires *Angew. Chem.* **124** 2781-4

[44] Tamaki Y, Furube A, Katoh R, Murai M, Hara K, Arakawa H and Tachiya M 2006 Trapping dynamics of electrons and holes in a nanocrystalline TiO2 film revealed by femtosecond visible/near-infrared transient absorption spectroscopy *C. R. Chim.* **9** 268-74

[45] Zarifi M H, Farsinezhad S, Abdolrazzaghi M, Daneshmand M and Shankar K 2016 Selective microwave sensors exploiting the interaction of analytes with trap states in TiO2 nanotube arrays *Nanoscale* **8** 7466-73

[46] Helmy R and Fadeev A Y 2002 Self-Assembled Monolayers Supported on TiO2: Comparison of C18H37SiX3 (X = H, Cl, OCH3), C18H37Si(CH3)2Cl, and C18H37PO(OH)2 *Langmuir* **18** 8924-8

[47] Liu H-B, Venkataraman N V, Spencer N D, Textor M and Xiao S-J 2008 Structural Evolution of Self-Assembled Alkanephosphate Monolayers on TiO2 *ChemPhysChem* **9** 1979-81

[48] Luschtinetz R, Frenzel J, Milek T and Seifert G 2009 Adsorption of Phosphonic Acid at the TiO2 Anatase (101) and Rutile (110) Surfaces *J. Phys. Chem. C* **113** 5730-40

[49] Kar P, Pandey A, Greer J J and Shankar K 2012 Ultrahigh sensitivity assays for human cardiac troponin I using TiO2 nanotube arrays *Lab Chip* **12** 821-8

[50] Zorn G, Gotman I, Gutmanas E Y, Adadi R, Salitra G and Sukenik C N 2005 Surface Modification of Ti45Nb Alloy with an Alkylphosphonic Acid Self-Assembled Monolayer *Chem. Mater.* **17** 4218-26

[51] Gao W, Dickinson L, Grozinger C, Morin F G and Reven L 1996 Self-Assembled Monolayers of Alkylphosphonic Acids on Metal Oxides *Langmuir* **12** 6429-35

[52] Gawalt E S, Lu G, Bernasek S L and Schwartz J 1999 Enhanced bonding of alkanephosphonic acids to oxidized titanium using surface-bound alkoxyzirconium complex interfaces *Langmuir* **15** 8929-33

[53] Hotchkiss P J, Jones S C, Paniagua S A, Sharma A, Kippelen B, Armstrong N R and Marder S R 2012 The Modification of Indium Tin Oxide with Phosphonic Acids: Mechanism of Binding, Tuning of Surface Properties, and Potential for Use in Organic Electronic Applications *Acc. Chem. Res.* **45** 337-46

[54] Zhang B, Kong T, Xu W, Su R, Gao Y and Cheng G 2010 Surface Functionalization of Zinc Oxide by Carboxyalkylphosphonic Acid Self-Assembled Monolayers *Langmuir* **26** 4514-22

[55] Many A and Rakavy G 1962 Theory of Transient Space-Charge-Limited Currents in Solids in the Presence of Trapping *Phys. Rev.* **126** 1980-8

[56] Kočka J, Klíma O, Juška G, Hoheisel M and Plättner R 1991 SCLC transients in a-Si: H—New features and possibilities *J. Non-Cryst. Solids* **137** 427-30

[57] Juška G, Viliunas M, Arlauskas K and Kočka J 1995 Space-charge-limited photocurrent transients: The influence of bimolecular recombination *Phys. Rev. B* **51** 16668

[58] Yamada Y and Kanemitsu Y 2012 Determination of electron and hole lifetimes of rutile and anatase TiO2 single crystals *Appl. Phys. Lett.* **101** 133907

SUPPLEMENTARY INFORMATION

100-Fold Improvement in Carrier Drift Mobilities in Alkanephosphonate-Passivated Monocrystalline TiO_2 Nanowire Arrays

A. Mohammadpour,[1*] B. D. Wiltshire,[1] Y. Zhang,[1] S. Farsinezhad,[1] A.M. Askar,[1] R. Kisslinger,[1] Y. Ren,[1] P. Kar[1] and K. Shankar[1, 2*]

[1]*Department of Electrical and Computer Engineering, University of Alberta, 9211 - 116 St, Edmonton, Alberta, Canada T6G 1H9*

[2]*NRC National Institute for Nanotechnology, 11421 Saskatchewan Dr NW, Edmonton, AB T6G 29*

***Authors to whom correspondence should be addressed:**

1. Arash Mohammadpour (arash3@ualberta.ca)

2. Karthik Shankar (kshankar@ualberta.ca)

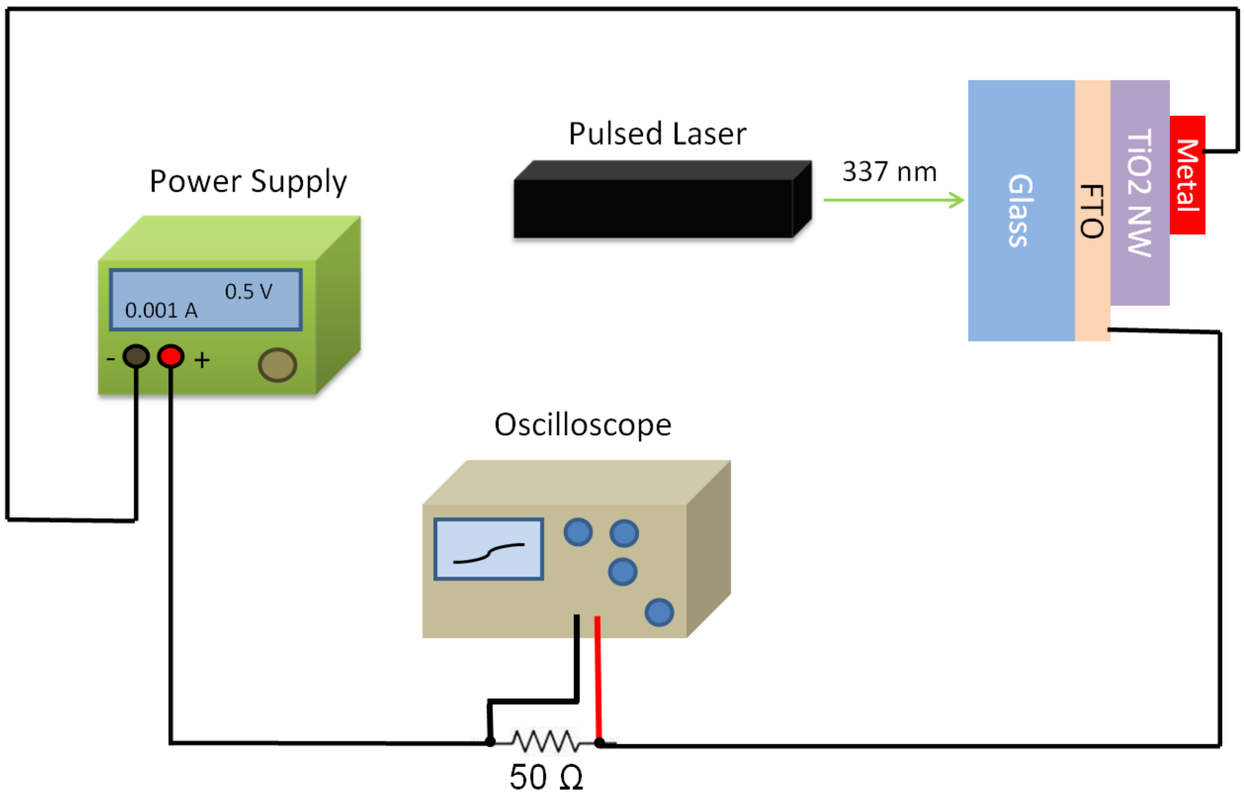

Figure S1. Schematic of the experimental configuration used for SCLC-TOF studies

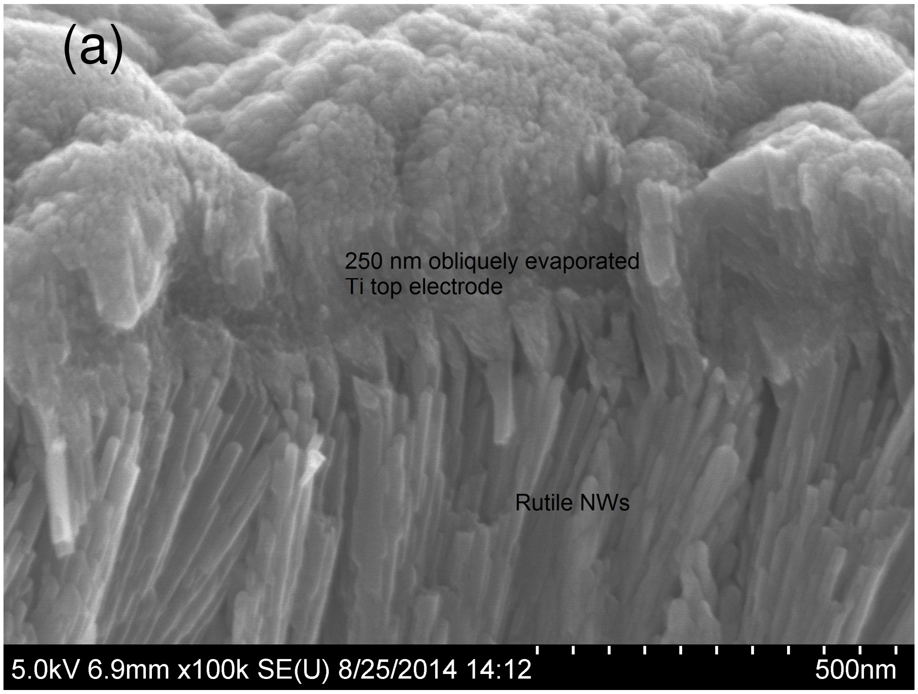

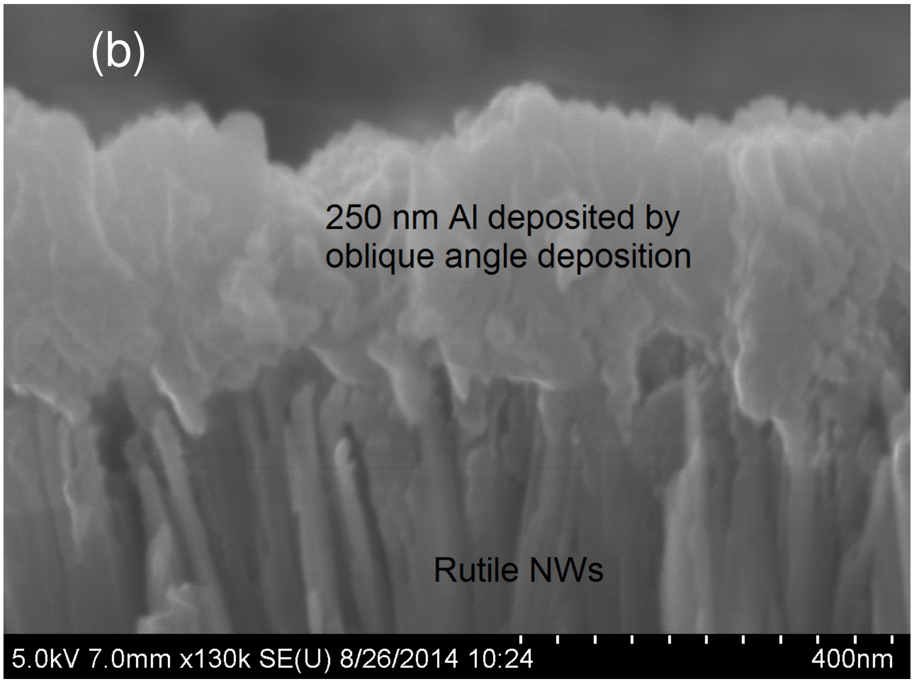

Figure S2. FESEM images of the results of (a) Ti and (b) Al metallization on Rut-NWA samples. Due to the use of obliquely angle deposition to deposit the top metal electrodes, penetration of the metal in between the nanowires was avoided.

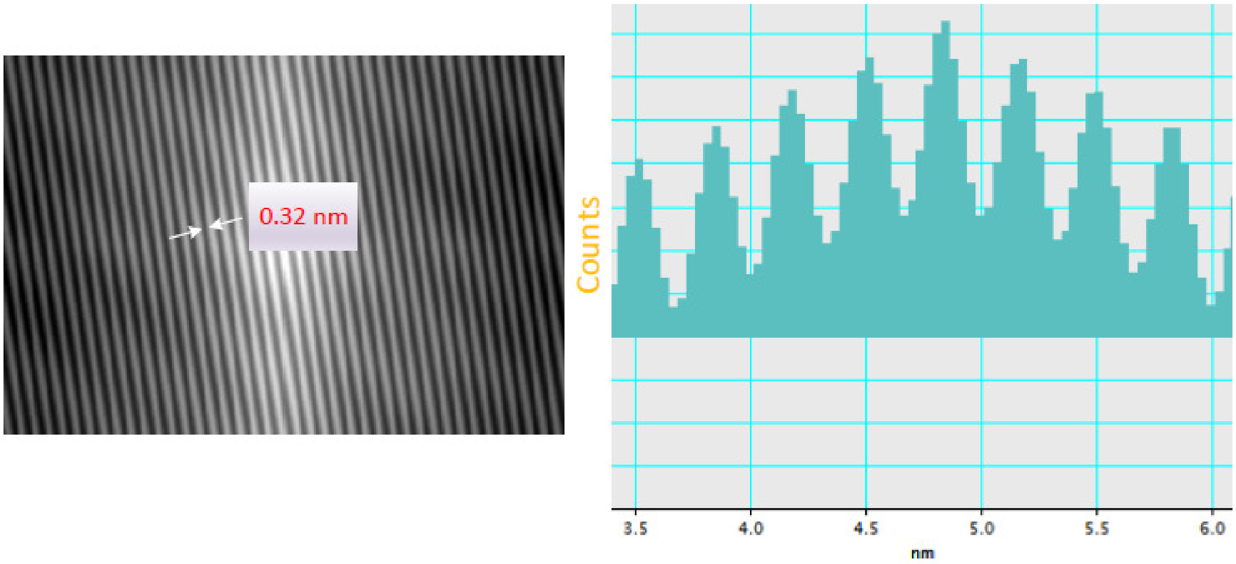

Figure S3. Estimation of the spacing of lattice fringes in the HRTEM image of Fig. 3a

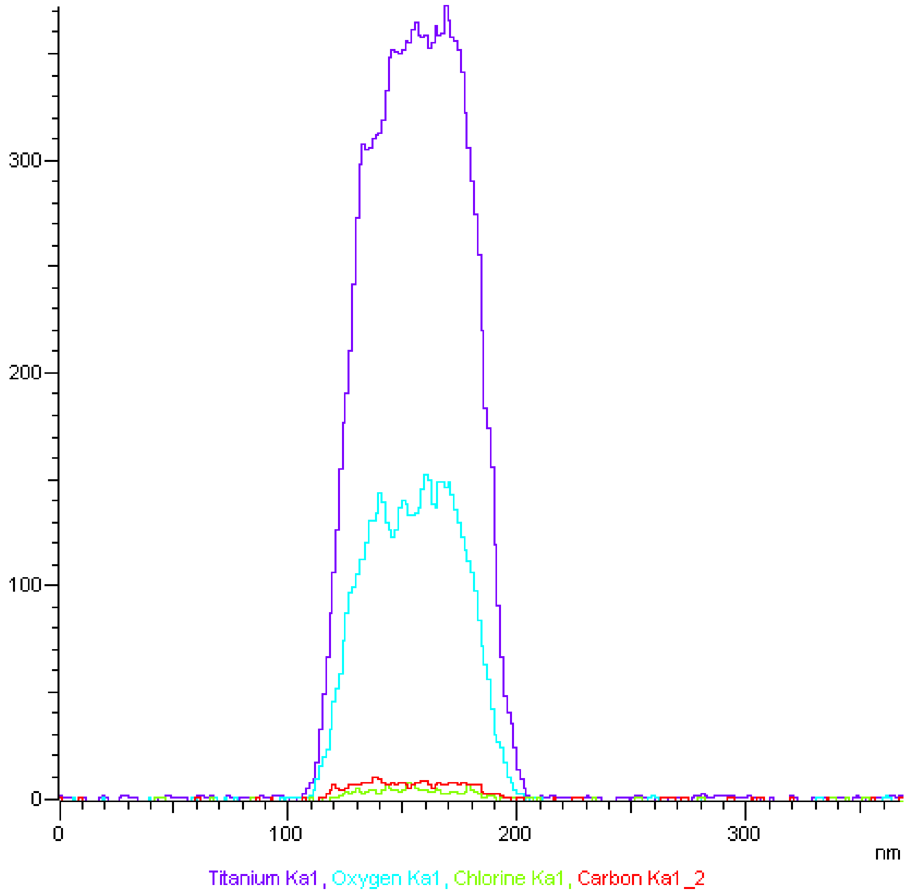

Figure S4. Results of TEM EDX line-scans of the Rut-NWAs shown in Fig. 3b for all elements

Section S1. Initial and final values of *j(t)* in SCLC-TOF measurements

The initial value (j_0) and maximum value (j_m) of the transient space charge limited photocurrent density can be used to estimate the carrier mobility from the expressions[1]

$$j_0 = \frac{\varepsilon \mu_n V^2}{2d^3} \qquad (1)$$

and

$$j_m = 2.72\frac{\varepsilon \mu_n V^2}{2d^3} \qquad (2)$$

Single crystal rutile is a highly anisotropic material. Since the nanowires are oriented along the [002] direction, the value of 159 for ε_r,||c-axis was used for the relative permittivity of Rut-NWAs.[2] While estimation of the mobility from Eqn (1) is most convenient, estimation of the mobility from Eqn (2) is most reliable; however the initial current j_0 is not always observable in the oscilloscope's small signal AC mode unless the initial transient current peak due to screening and system response time delays has a very fast decay in comparison to the carrier transit time. While a maximum in the current is nearly always observed, the use of Eqn (3) is the least reliable method due to the trapping- and recombination-mediated decrease in the current maxima. However, the maximum current, when it exists and clearly attributable to carrier transit, can be used to place a lower bound on the mobility estimate.

Section S2. Relationship of t_{cusp} to transit time in dark injection

In dark injection-type transient SCLC measurements, the maximum charge injected by the voltage pulse is limited to *CV* where *C* is the sample capacitance and *V* is the peak magnitude of the applied pulse. This is in contrast to SCLC-TOF measurements wherein the photoinjected charge can be orders of magnitude greater than *CV*. Only majority carrier transport may be probed in dark injection measurements. The transit time is given by $0.786 \times \boldsymbol{t_{cusp}}$, due to which the electron mobility is given by

$$\mu_n = 0.786 \frac{d^2}{V t_{cusp}} \qquad (3)$$

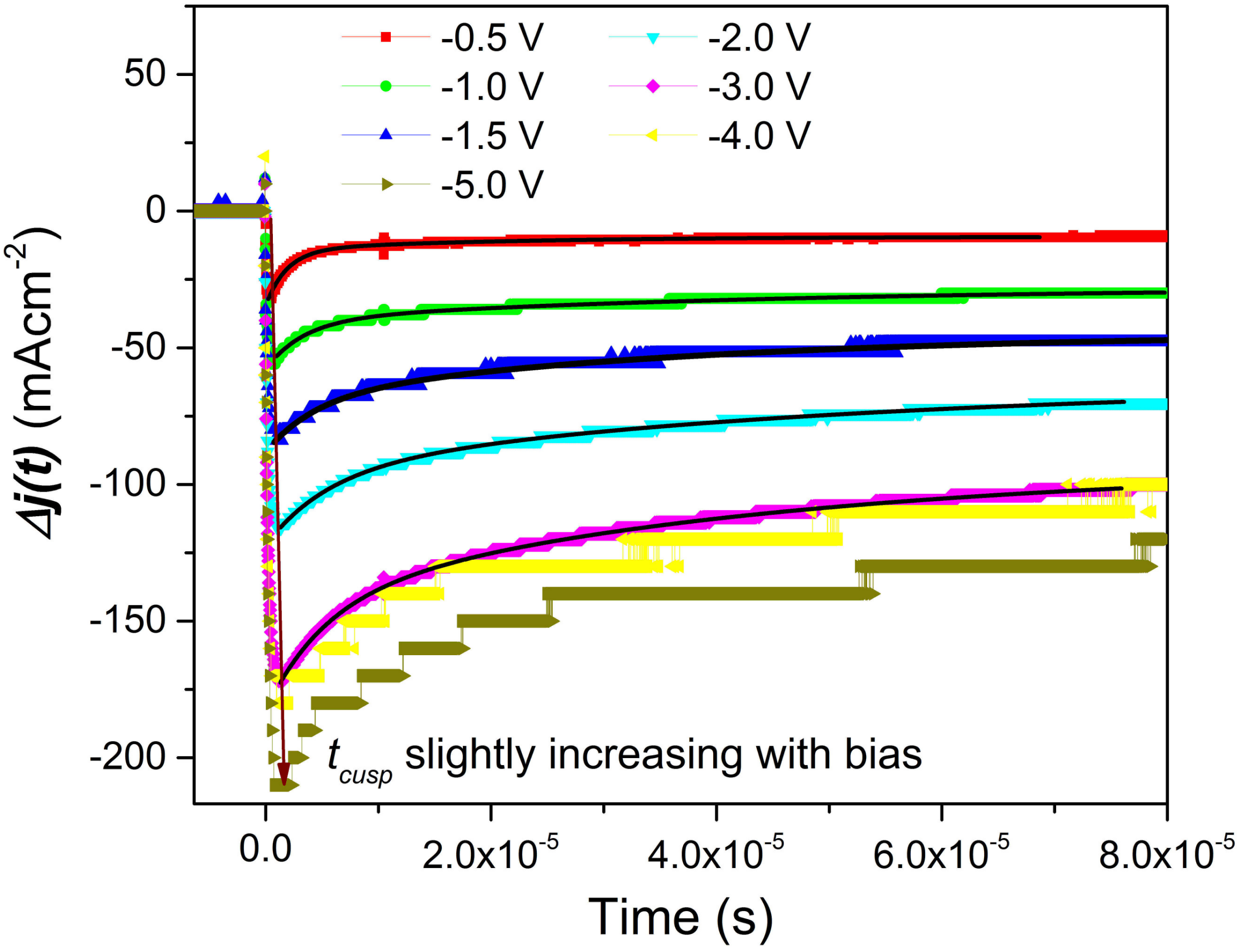

Figure S5. SCLC photocurrent transients for different values of negative bias applied to Pt top electrode following the irradiation of ODPA-coated Rut-NWAs by a 4 ns optical pulse from a N_2 laser. For bias values of -0.5 V to -3 V, the post-transit transient photocurrents were fitted to biexponential decays, which are shown as solid black lines. For all the fitted decays, the range of the faster component was 1.9-5.2 × 10^{-6} s while the slower component had a range of 1.9-4.7 × 10^{-5} s.

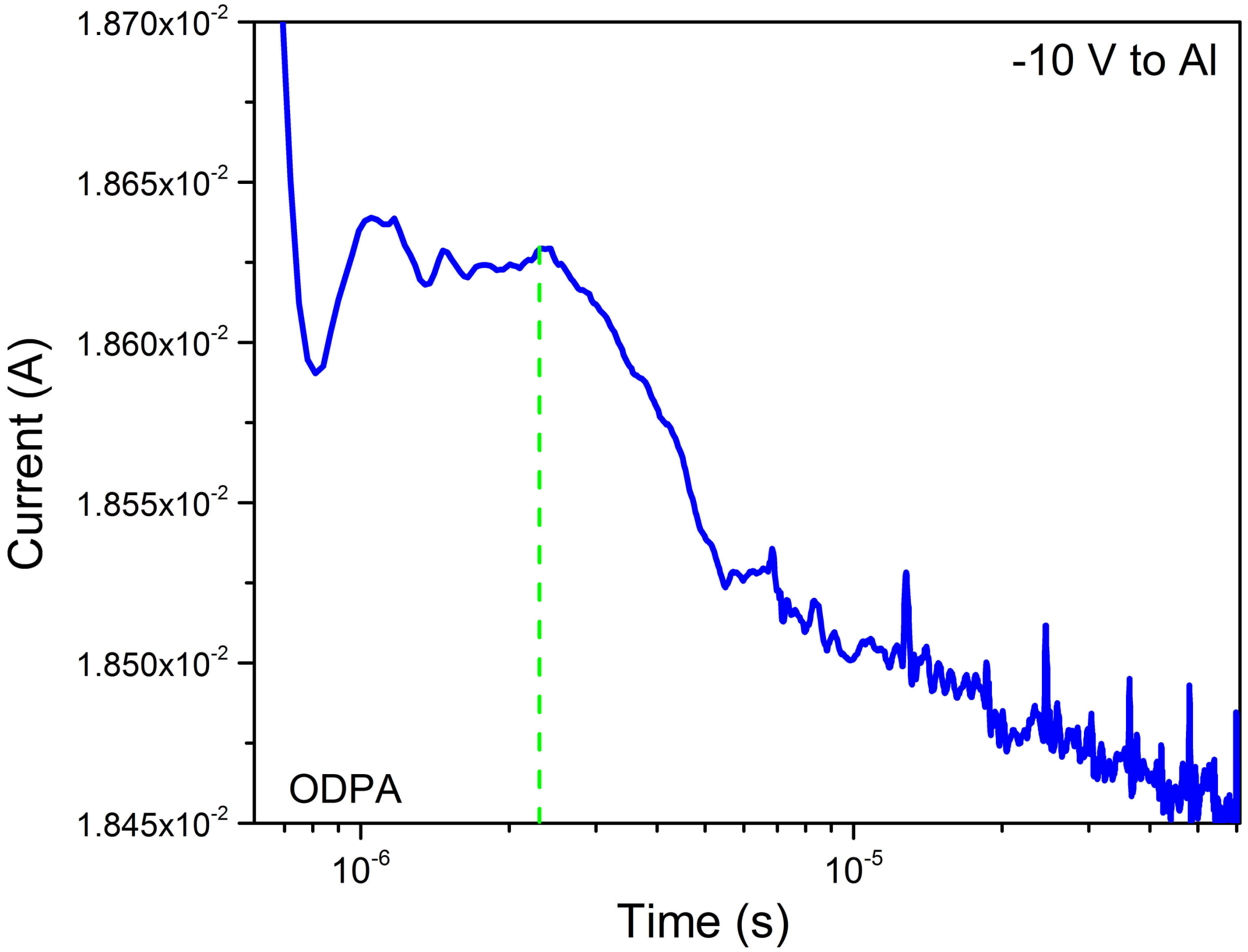

Figure S6. Dark injection current transient for ODPA-coated nanowires with Al top metal electrode at negative potentials.

REFERENCES

1. A. Many and G. Rakavy, *Phys. Rev.*, 1962, **126**, 1980-1988.
2. M. E. Tobar, J. Krupka, E. N. Ivanov and R. A. Woode, *J. Appl. Phys.*, 1998, **83**, 1604-1609.